Production properties of deuterons, tritons, and ^{3}He via an analytical nucleon coalescence method in Pb-Pb collisions at $\sqrt{s_{NN}} = 2.76$ TeV

Rui-Qin Wang,[1] Yan-Hao Li,[1] Jun Song,[2] and Feng-Lan Shao[1,*]

[1]*School of Physics and Physical Engineering, Qufu Normal University, Shandong 273165, China*

[2]*School of Physical Science and Intelligent Engineering, Jining University, Shandong 273155, China*

(Received 3 October 2023; accepted 23 February 2024; published 13 March 2024)

We improve a nucleon coalescence model to include the coordinate-momentum correlation in nucleon joint distributions, and apply it to Pb-Pb collisions at $\sqrt{s_{NN}} = 2.76$ TeV to study production properties of deuterons (d), helions (^{3}He), and tritons (t). We give formulas of the coalescence factors B_2 and B_3, and naturally explain their behaviors as functions of the collision centrality and the transverse momentum per nucleon p_T/A. We reproduce the transverse momentum spectra, averaged transverse momenta, and yield rapidity densities of d, ^{3}He, and t, and find the system effective radius obtained in the coalescence production of light nuclei behaves similarly to Hanbury Brown–Twiss interferometry radius. We particularly give expressions of yield ratios d/p, $^3\mathrm{He}/d$, t/p, $^3\mathrm{He}/p$, d/p^2, $^3\mathrm{He}/p^3$, $t/^3\mathrm{He}$ and argue their nontrivial behaviors can be used to distinguish production mechanisms of light nuclei.

DOI: 10.1103/PhysRevC.109.034907

I. INTRODUCTION

In ultrarelativistic heavy ion collisions, light nuclei such as deuterons (d), helions (^{3}He), and tritons (t) are a special group of observables [1–13]. They are composite clusters and their production mechanisms are still under debate so far. As most of them are formed at the late stage of the system evolution, light nuclei are considered as sensitive probes of the fireball freeze-out properties [1–5]. The study of light nuclei production can help understand many fundamental issues in relativistic heavy ion collision physics, e.g., the hadronization mechanism [6], the structure of the quantum chromodynamics phase diagram [7–11], and the search for dibaryons and other molecular states [12,13].

In recent decades, the production of light nuclei in ultrarelativistic heavy ion collisions has always attracted much attention both in experiment [14–24] and in theory [25–31]. The STAR experiment at the BNL Relativistic Heavy Ion Collider (RHIC) and the ALICE experiment at the CERN Large Hadron Collider (LHC) have collected a wealth of data on light nuclei production. These data exhibit some fascinating features [18–24]. In theory two production mechanisms, the thermal production mechanism [30,32–35] and the coalescence mechanism [27,28,36–45], have proved to be successful in describing light nuclei formation. In addition, transport scenario [46–52] is employed to study how light nuclei evolve and survive during the hadronic system evolution.

The coalescence mechanism, in which light nuclei are assumed to be produced by the coalescence of the jacent nucleons in the phase space, possesses its unique characteristics. In order to see whether, if so, to what extent, these characteristics depend on the particular coalescence model used in obtaining these characteristics, we, in our previous works [53–55], developed an analytic description for the production of different species of light nuclei in the coalescence picture with the assumption of the coordinate-momentum factorization. The obtained analytic formulas clearly show the relationships of light nuclei with primordial nucleons and effects of different factors on light nuclei production such as the whole hadronic system scale as well as the sizes of the formed light nuclei. In Refs. [53,54], we applied the analytic coalescence model to Au-Au collisions at RHIC energies to successfully explain the transverse momentum spectra, yield rapidity densities, averaged transverse momenta and yield correlations of different light nuclei. We also applied it to pp, p-Pb, and Pb-Pb collisions at LHC to study the behavior of the coalescence factor B_A [55], and found it can naturally explain the relatively weak p_T dependence of B_A in pp and p-Pb collisions. In Pb-Pb collisions it gave qualitative growth of B_A against p_T, but growth extent was underestimated. It is urgently necessary to give quantitative explanations for B_A and further explore intrinsic properties of light nuclei production in heavy ion collisions with such high collision energy at the LHC.

In this work, we extend the nucleon coalescence model to include the coordinate-momentum correlation originating possibly from the collective flows [56], the temperature gradients [57], etc., and apply it to Pb-Pb collisions at LHC to study the production of light nuclei. One main goal of this article is to bring to light the characteristics originating from the nucleon coalescence itself and to discriminate influences of different factors in heavy ion collisions with so high collision energy on light nuclei production. We study coalescence factors (B_2 and B_3), transverse momentum (p_T) spectra, averaged transverse momenta ($\langle p_T \rangle$), yield rapidity

*shaofl@mail.sdu.edu.cn

densities (dN/dy), and yield ratios of different species of light nuclei. We find the nucleon coalescence model including the coordinate-momentum correlation can well describe the light nuclei production in Pb-Pb collisions at $\sqrt{s_{NN}} = 2.76$ TeV. We also find the system effective radius obtained in the coalescence production of light nuclei behaves similarly to Hanbury Brown–Twiss (HBT) interferometry radius.

The paper is organized as follows. In Sec. II we give an introduction to the nucleon coalescence model. In Sec. III we study coalescence factors B_2 and B_3, and discuss their behaviors as functions of the collision centrality and the transverse momentum per nucleon. In Sec. IV, we study the p_T spectra, averaged transverse momenta, yield rapidity densities and yield ratios of d, ^{3}He, and t. In Sec. V we give our summary.

II. THE NUCLEON COALESCENCE MODEL

In this section we extend the nucleon coalescence model in our previous works [53–55] to include the coordinate-momentum correlation in nucleon joint distributions. The current nucleon coalescence model is a static and effective model. The nucleon coalescence is executed on an equivalent kinetic freeze-out surface which is formed from different times. The finite emission duration is absorbed in an effective volume parameter. This dealing method makes the analytic and intuitive insights possible. We present a formulism of two nucleons coalescing into d and that of three nucleons coalescing into ^{3}He and t. For t, the deduction process is the same as that of ^{3}He and we do not repeat the display and only give the final formula.

We start from a hadronic system produced at the final stage of the evolution of high energy heavy ion collision and suppose light nuclei are formed via the nucleon coalescence. The three-dimensional momentum distribution of the produced deuterons $f_d(\boldsymbol{p})$ and that of helions $f_{^3\mathrm{He}}(\boldsymbol{p})$ are

$$f_d(\boldsymbol{p}) = N_{pn}\int d\boldsymbol{x}_1 d\boldsymbol{x}_2 d\boldsymbol{p}_1 d\boldsymbol{p}_2 f_{pn}^{(n)}(\boldsymbol{x}_1,\boldsymbol{x}_2;\boldsymbol{p}_1,\boldsymbol{p}_2) \times \mathcal{R}_d(\boldsymbol{x}_1,\boldsymbol{x}_2;\boldsymbol{p}_1,\boldsymbol{p}_2,\boldsymbol{p}), \quad (1)$$

$$f_{^3\mathrm{He}}(\boldsymbol{p}) = N_{ppn}\int d\boldsymbol{x}_1 d\boldsymbol{x}_2 d\boldsymbol{x}_3 d\boldsymbol{p}_1 d\boldsymbol{p}_2 d\boldsymbol{p}_3 \times f_{ppn}^{(n)}(\boldsymbol{x}_1,\boldsymbol{x}_2,\boldsymbol{x}_3;\boldsymbol{p}_1,\boldsymbol{p}_2,\boldsymbol{p}_3) \times \mathcal{R}_{^3\mathrm{He}}(\boldsymbol{x}_1,\boldsymbol{x}_2,\boldsymbol{x}_3;\boldsymbol{p}_1,\boldsymbol{p}_2,\boldsymbol{p}_3,\boldsymbol{p}). \quad (2)$$

Here, $f_{pn}^{(n)}(\boldsymbol{x}_1,\boldsymbol{x}_2;\boldsymbol{p}_1,\boldsymbol{p}_2)$ is the normalized joint coordinate-momentum distribution of proton-neutron pairs and $f_{ppn}^{(n)}(\boldsymbol{x}_1,\boldsymbol{x}_2,\boldsymbol{x}_3;\boldsymbol{p}_1,\boldsymbol{p}_2,\boldsymbol{p}_3)$ is that of three-nucleon clusters. $N_{pn} = N_p N_n$ is the number of all possible pn pairs and $N_{ppn} = N_p(N_p-1)N_n$ is that of all possible ppn-clusters. N_p is the proton number and N_n is the neutron number in the considered hadronic system. $\mathcal{R}_d(\boldsymbol{x}_1,\boldsymbol{x}_2;\boldsymbol{p}_1,\boldsymbol{p}_2,\boldsymbol{p})$ and $\mathcal{R}_{^3\mathrm{He}}(\boldsymbol{x}_1,\boldsymbol{x}_2,\boldsymbol{x}_3;\boldsymbol{p}_1,\boldsymbol{p}_2,\boldsymbol{p}_3,\boldsymbol{p})$ are kernel functions. Here, and from now on, we use boldface type to distinguish three-dimensional vectors.

Taking into account constraints from the momentum conservation and intrinsic quantum numbers of light nuclei, we rewrite kernel functions in the following forms as in Refs. [53–55,58]:

$$\mathcal{R}_d(\boldsymbol{x}_1,\boldsymbol{x}_2;\boldsymbol{p}_1,\boldsymbol{p}_2,\boldsymbol{p}) = g_d\mathcal{R}_d^{(x,p)}(\boldsymbol{x}_1,\boldsymbol{x}_2;\boldsymbol{p}_1,\boldsymbol{p}_2)\delta\left(\sum_{i=1}^{2}\boldsymbol{p}_i - \boldsymbol{p}\right), \quad (3)$$

$$\mathcal{R}_{^3\mathrm{He}}(\boldsymbol{x}_1,\boldsymbol{x}_2,\boldsymbol{x}_3;\boldsymbol{p}_1,\boldsymbol{p}_2,\boldsymbol{p}_3,\boldsymbol{p}) = g_{^3\mathrm{He}}\mathcal{R}_{^3\mathrm{He}}^{(x,p)}(\boldsymbol{x}_1,\boldsymbol{x}_2,\boldsymbol{x}_3;\boldsymbol{p}_1,\boldsymbol{p}_2,\boldsymbol{p}_3)\delta\left(\sum_{i=1}^{3}\boldsymbol{p}_i - \boldsymbol{p}\right), \quad (4)$$

where the spin degeneracy factors $g_d = 3/4$ and $g_{^3\mathrm{He}} = 1/4$. The Dirac δ functions guarantee the momentum conservation in the coalescence process. The remaining $\mathcal{R}_d^{(x,p)}(\boldsymbol{x}_1,\boldsymbol{x}_2;\boldsymbol{p}_1,\boldsymbol{p}_2)$ and $\mathcal{R}_{^3\mathrm{He}}^{(x,p)}(\boldsymbol{x}_1,\boldsymbol{x}_2,\boldsymbol{x}_3;\boldsymbol{p}_1,\boldsymbol{p}_2,\boldsymbol{p}_3)$ can be solved from the Wigner transformation as adopting the wave function of a spherical harmonic oscillator as in Refs. [59,60]. They are as follows:

$$\mathcal{R}_d^{(x,p)}(\boldsymbol{x}_1,\boldsymbol{x}_2;\boldsymbol{p}_1,\boldsymbol{p}_2) = 8e^{-\frac{(x_1'-x_2')^2}{\sigma_d^2}}e^{-\frac{\sigma_d^2(p_1'-p_2')^2}{4\hbar^2c^2}}, \quad (5)$$

$$\mathcal{R}_{^3\mathrm{He}}^{(x,p)}(\boldsymbol{x}_1,\boldsymbol{x}_2,\boldsymbol{x}_3;\boldsymbol{p}_1,\boldsymbol{p}_2,\boldsymbol{p}_3) = 8^2 e^{-\frac{(x_1'-x_2')^2}{2\sigma_{^3\mathrm{He}}^2}}e^{-\frac{(x_1'+x_2'-2x_3')^2}{6\sigma_{^3\mathrm{He}}^2}} \times e^{-\frac{\sigma_{^3\mathrm{He}}^2(p_1'-p_2')^2}{2\hbar^2c^2}}e^{-\frac{\sigma_{^3\mathrm{He}}^2(p_1'+p_2'-2p_3')^2}{6\hbar^2c^2}}. \quad (6)$$

The superscript "′" in the coordinate or momentum variable denotes the nucleon coordinate or momentum in the rest frame of the pn pair or ppn cluster. The width parameter $\sigma_d = \sqrt{\frac{8}{3}}R_d$ and $\sigma_{^3\mathrm{He}} = R_{^3\mathrm{He}}$, where $R_d = 2.1421$ fm and $R_{^3\mathrm{He}} = 1.9661$ fm are the root-mean-square radius of the deuteron and that of the ^{3}He, respectively [61]. The factor $\hbar c$ comes from the used GeV fm unit, and it is 0.197 GeV fm.

As we know, profiles of nuclei wave functions generally affect their productions in the coalescence picture, especially in relatively small reaction systems, e.g., peripheral Pb-Pb, p-Pb, and pp collisions or for larger nuclei, e.g., the hypertriton. In Ref. [62], different wave functions, e.g., the spherical harmonic oscillator wave function and the Hulthen wave function, have been employed to study nuclei production and found results from these wave functions are roughly consistent at $R_f > 2$ fm which is the relevant region in our current Pb-Pb collisions. Considering the wave function of a spherical harmonic oscillator is particularly tractable and useful for analytic insight, we adopt this profile.

Substituting Eqs. (3)–(6) into Eqs. (1) and (2), we have

$$f_d(\boldsymbol{p}) = g_d N_{pn}\int d\boldsymbol{x}_1 d\boldsymbol{x}_2 d\boldsymbol{p}_1 d\boldsymbol{p}_2 f_{pn}^{(n)}(\boldsymbol{x}_1,\boldsymbol{x}_2;\boldsymbol{p}_1,\boldsymbol{p}_2) 8e^{-\frac{(x_1'-x_2')^2}{\sigma_d^2}}e^{-\frac{\sigma_d^2(p_1'-p_2')^2}{4\hbar^2c^2}}\delta\left(\sum_{i=1}^{2}\boldsymbol{p}_i - \boldsymbol{p}\right), \quad (7)$$

$$f_{^3\mathrm{He}}(\boldsymbol{p}) = g_{^3\mathrm{He}} N_{ppn} \int d\boldsymbol{x}_1 d\boldsymbol{x}_2 d\boldsymbol{x}_3 d\boldsymbol{p}_1 d\boldsymbol{p}_2 d\boldsymbol{p}_3 f^{(n)}_{ppn}(\boldsymbol{x}_1, \boldsymbol{x}_2, \boldsymbol{x}_3; \boldsymbol{p}_1, \boldsymbol{p}_2, \boldsymbol{p}_3) \delta\left(\sum_{i=1}^{3} \boldsymbol{p}_i - \boldsymbol{p}\right)$$
$$\times 8^2 e^{-\frac{(x'_1 - x'_2)^2}{2\sigma^2_{^3\mathrm{He}}}} e^{-\frac{(x'_1 + x'_2 - 2x'_3)^2}{6\sigma^2_{^3\mathrm{He}}}} e^{-\frac{\sigma^2_{^3\mathrm{He}}(p'_1 - p'_2)^2}{2\hbar^2 c^2}} e^{-\frac{\sigma^2_{^3\mathrm{He}}(p'_1 + p'_2 - 2p'_3)^2}{6\hbar^2 c^2}}. \tag{8}$$

Considering that the gaussian width values $2\hbar c/\sigma_d$, $\sqrt{2}\hbar c/\sigma_{^3\mathrm{He}}$, and $\sqrt{6}\hbar c/\sigma_{^3\mathrm{He}}$ in the momentum-dependent kernel functions are quite small, we mathematically approximate the gaussian form $e^{-(\Delta \boldsymbol{p}')^2/\epsilon^2}$ as $(\sqrt{\pi}\epsilon)^3 \delta(\Delta \boldsymbol{p}')$, where ϵ is a small quantity. Then we can obtain

$$\begin{aligned} f_d(\boldsymbol{p}) &= 8 g_d N_{pn} \int d\boldsymbol{x}_1 d\boldsymbol{x}_2 d\boldsymbol{p}_1 d\boldsymbol{p}_2 f^{(n)}_{pn}(\boldsymbol{x}_1, \boldsymbol{x}_2; \boldsymbol{p}_1, \boldsymbol{p}_2) e^{-\frac{(x'_1 - x'_2)^2}{\sigma_d^2}} \left(\frac{2\hbar c\sqrt{\pi}}{\sigma_d}\right)^3 \delta(\boldsymbol{p}'_1 - \boldsymbol{p}'_2) \delta\left(\sum_{i=1}^{2} \boldsymbol{p}_i - \boldsymbol{p}\right) \\ &= 8 g_d N_{pn} \int d\boldsymbol{x}_1 d\boldsymbol{x}_2 d\boldsymbol{p}_1 d\boldsymbol{p}_2 f^{(n)}_{pn}(\boldsymbol{x}_1, \boldsymbol{x}_2; \boldsymbol{p}_1, \boldsymbol{p}_2) e^{-\frac{(x'_1 - x'_2)^2}{\sigma_d^2}} \left(\frac{2\hbar c\sqrt{\pi}}{\sigma_d}\right)^3 \gamma \delta(\boldsymbol{p}_1 - \boldsymbol{p}_2) \delta\left(\sum_{i=1}^{2} \boldsymbol{p}_i - \boldsymbol{p}\right) \\ &= 8 g_d N_{pn} \left(\frac{\hbar c\sqrt{\pi}}{\sigma_d}\right)^3 \gamma \int d\boldsymbol{x}_1 d\boldsymbol{x}_2 f^{(n)}_{pn}\left(\boldsymbol{x}_1, \boldsymbol{x}_2; \frac{\boldsymbol{p}}{2}, \frac{\boldsymbol{p}}{2}\right) e^{-\frac{(x'_1 - x'_2)^2}{\sigma_d^2}}, \end{aligned} \tag{9}$$

where the Lorentz contraction factor γ comes from the Lorentz transformation $\Delta \boldsymbol{p}' = \frac{1}{\gamma} \Delta \boldsymbol{p}$. Similarly for ^{3}He we have

$$f_{^3\mathrm{He}}(\boldsymbol{p}) = 8^2 g_{^3\mathrm{He}} N_{ppn} \left(\frac{\hbar^2 c^2 \pi}{\sqrt{3}\sigma^2_{^3\mathrm{He}}}\right)^3 \gamma^2 \int d\boldsymbol{x}_1 d\boldsymbol{x}_2 d\boldsymbol{x}_3 f^{(n)}_{ppn}\left(\boldsymbol{x}_1, \boldsymbol{x}_2, \boldsymbol{x}_3; \frac{\boldsymbol{p}}{3}, \frac{\boldsymbol{p}}{3}, \frac{\boldsymbol{p}}{3}\right) e^{-\frac{(x'_1 - x'_2)^2}{2\sigma^2_{^3\mathrm{He}}}} e^{-\frac{(x'_1 + x'_2 - 2x'_3)^2}{6\sigma^2_{^3\mathrm{He}}}}. \tag{10}$$

Changing coordinate integral variables in Eq. (9) to be $\boldsymbol{X} = \frac{\boldsymbol{x}_1 + \boldsymbol{x}_2}{2}$ and $\boldsymbol{r} = \boldsymbol{x}_1 - \boldsymbol{x}_2$, and those in Eq. (10) to be $\boldsymbol{Y} = (\boldsymbol{x}_1 + \boldsymbol{x}_2 + \boldsymbol{x}_3)/\sqrt{3}$, $\boldsymbol{r}_1 = (\boldsymbol{x}_1 - \boldsymbol{x}_2)/\sqrt{2}$ and $\boldsymbol{r}_2 = (\boldsymbol{x}_1 + \boldsymbol{x}_2 - 2\boldsymbol{x}_3)/\sqrt{6}$, we have

$$f_d(\boldsymbol{p}) = 8 g_d N_{pn} \left(\frac{\hbar c\sqrt{\pi}}{\sigma_d}\right)^3 \gamma \int d\boldsymbol{X} d\boldsymbol{r} f^{(n)}_{pn}\left(\boldsymbol{X}, \boldsymbol{r}; \frac{\boldsymbol{p}}{2}, \frac{\boldsymbol{p}}{2}\right) e^{-\frac{r'^2}{\sigma_d^2}}, \tag{11}$$

$$f_{^3\mathrm{He}}(\boldsymbol{p}) = 8^2 g_{^3\mathrm{He}} N_{ppn} \left(\frac{\hbar^2 c^2 \pi}{\sqrt{3}\sigma^2_{^3\mathrm{He}}}\right)^3 \gamma^2 \int d\boldsymbol{Y} d\boldsymbol{r}_1 d\boldsymbol{r}_2 f^{(n)}_{ppn}\left(\boldsymbol{Y}, \boldsymbol{r}_1, \boldsymbol{r}_2; \frac{\boldsymbol{p}}{3}, \frac{\boldsymbol{p}}{3}, \frac{\boldsymbol{p}}{3}\right) e^{-\frac{r'^2_1}{\sigma^2_{^3\mathrm{He}}}} e^{-\frac{r'^2_2}{\sigma^2_{^3\mathrm{He}}}}. \tag{12}$$

Considering the nucleon strong interaction and the nucleon coalescence are local, we neglect the effect of collective motion on the center of mass coordinate and assume it is factorized in nucleon joint distributions, i.e.,

$$f^{(n)}_{pn}\left(\boldsymbol{X}, \boldsymbol{r}; \frac{\boldsymbol{p}}{2}, \frac{\boldsymbol{p}}{2}\right) = f^{(n)}_{pn}(\boldsymbol{X}) f^{(n)}_{pn}\left(\boldsymbol{r}; \frac{\boldsymbol{p}}{2}, \frac{\boldsymbol{p}}{2}\right), \tag{13}$$

$$f^{(n)}_{ppn}\left(\boldsymbol{Y}, \boldsymbol{r}_1, \boldsymbol{r}_2; \frac{\boldsymbol{p}}{3}, \frac{\boldsymbol{p}}{3}, \frac{\boldsymbol{p}}{3}\right) = f^{(n)}_{ppn}(\boldsymbol{Y}) f^{(n)}_{ppn}\left(\boldsymbol{r}_1, \boldsymbol{r}_2; \frac{\boldsymbol{p}}{3}, \frac{\boldsymbol{p}}{3}, \frac{\boldsymbol{p}}{3}\right). \tag{14}$$

Then we have

$$f_d(\boldsymbol{p}) = 8 g_d N_{pn} \left(\frac{\hbar c\sqrt{\pi}}{\sigma_d}\right)^3 \gamma \int d\boldsymbol{r} f^{(n)}_{pn}\left(\boldsymbol{r}; \frac{\boldsymbol{p}}{2}, \frac{\boldsymbol{p}}{2}\right) e^{-\frac{r'^2}{\sigma_d^2}}, \tag{15}$$

$$f_{^3\mathrm{He}}(\boldsymbol{p}) = 8^2 g_{^3\mathrm{He}} N_{ppn} \left(\frac{\hbar^2 c^2 \pi}{\sqrt{3}\sigma^2_{^3\mathrm{He}}}\right)^3 \gamma^2 \int d\boldsymbol{r}_1 d\boldsymbol{r}_2 f^{(n)}_{ppn}\left(\boldsymbol{r}_1, \boldsymbol{r}_2; \frac{\boldsymbol{p}}{3}, \frac{\boldsymbol{p}}{3}, \frac{\boldsymbol{p}}{3}\right) e^{-\frac{r'^2_1}{\sigma^2_{^3\mathrm{He}}}} e^{-\frac{r'^2_2}{\sigma^2_{^3\mathrm{He}}}}. \tag{16}$$

We adopt the frequently-used gaussian form for the relative coordinate distribution as in such as Ref. [63], i.e.,

$$f^{(n)}_{pn}\left(\boldsymbol{r}; \frac{\boldsymbol{p}}{2}, \frac{\boldsymbol{p}}{2}\right) = \frac{1}{\left[\pi C R_f^2(\boldsymbol{p})\right]^{3/2}} e^{-\frac{r^2}{C R_f^2(\boldsymbol{p})}} f^{(n)}_{pn}\left(\frac{\boldsymbol{p}}{2}, \frac{\boldsymbol{p}}{2}\right), \tag{17}$$

$$f^{(n)}_{ppn}\left(\boldsymbol{r}_1, \boldsymbol{r}_2; \frac{\boldsymbol{p}}{3}, \frac{\boldsymbol{p}}{3}, \frac{\boldsymbol{p}}{3}\right) = \frac{1}{\left[\pi^2 C_1 C_2 R_f^4(\boldsymbol{p})\right]^{3/2}} e^{-\frac{r_1^2}{C_1 R_f^2(\boldsymbol{p})}} e^{-\frac{r_2^2}{C_2 R_f^2(\boldsymbol{p})}} f^{(n)}_{ppn}\left(\frac{\boldsymbol{p}}{3}, \frac{\boldsymbol{p}}{3}, \frac{\boldsymbol{p}}{3}\right). \tag{18}$$

Here, $R_f(\boldsymbol{p})$ is the effective radius of the source system at the light nuclei freeze-out, and it generally depends on the momentum [64–66]. Considering relations between $\boldsymbol{r}$, $\boldsymbol{r}_1$, and $\boldsymbol{r}_2$ with $\boldsymbol{x}_1$, $\boldsymbol{x}_2$, and $\boldsymbol{x}_3$, C_1 equals to $C/2$ and C_2 equals to $2C/3$. So there is only one distribution width parameter C to be determined, and it is set to be 4 the same as that in Ref. [63]. Gaussian profile of

the relative coordinate distribution is convenient for analytical calculations, and there are some empirical arguments in favor of such choice [67,68].

With instantaneous coalescence in the rest frame of *pn* pair or *ppn* cluster, i.e., $\Delta t' = 0$, we get the Lorentz transformation

$$\boldsymbol{r} = \boldsymbol{r}' + (\gamma - 1)\frac{\boldsymbol{r}' \cdot \boldsymbol{\beta}}{\beta^2}\boldsymbol{\beta}, \tag{19}$$

where $\boldsymbol{\beta}$ is the three-dimensional velocity vector of the center-of-mass frame of *pn* pair or *ppn* cluster in the laboratory frame. Substituting Eqs. (17) and (18) into Eqs. (15) and (16) and using Eq. (19) to integrate from relative coordinate variables, we can obtain

$$f_d(\boldsymbol{p}) = \frac{8g_d(\sqrt{\pi}\hbar c)^3\gamma}{\left[CR_f^2(\boldsymbol{p}) + \sigma_d^2\right]\sqrt{C[R_f(\boldsymbol{p})/\gamma]^2 + \sigma_d^2}} f_{pn}\left(\frac{\boldsymbol{p}}{2}, \frac{\boldsymbol{p}}{2}\right), \tag{20}$$

$$f_{^3\mathrm{He}}(\boldsymbol{p}) = \frac{8^2 g_{^3\mathrm{He}}(\pi\hbar^2c^2)^3\gamma^2}{3\sqrt{3}\left[\frac{C}{2}R_f^2(\boldsymbol{p}) + \sigma_{^3\mathrm{He}}^2\right]\sqrt{\frac{C}{2}[R_f(\boldsymbol{p})/\gamma]^2 + \sigma_{^3\mathrm{He}}^2}} \frac{1}{\left[\frac{2C}{3}R_f^2(\boldsymbol{p}) + \sigma_{^3\mathrm{He}}^2\right]\sqrt{\frac{2C}{3}[R_f(\boldsymbol{p})/\gamma]^2 + \sigma_{^3\mathrm{He}}^2}} f_{ppn}\left(\frac{\boldsymbol{p}}{3}, \frac{\boldsymbol{p}}{3}, \frac{\boldsymbol{p}}{3}\right). \tag{21}$$

Ignoring correlations between protons and neutrons, we have the three-dimensional momentum distributions of light nuclei as

$$f_d(\boldsymbol{p}) = \frac{8g_d(\sqrt{\pi}\hbar c)^3\gamma}{\left[CR_f^2(\boldsymbol{p}) + \sigma_d^2\right]\sqrt{C[R_f(\boldsymbol{p})/\gamma]^2 + \sigma_d^2}} f_p\left(\frac{\boldsymbol{p}}{2}\right) f_n\left(\frac{\boldsymbol{p}}{2}\right), \tag{22}$$

$$f_{^3\mathrm{He}}(\boldsymbol{p}) = \frac{8^2 g_{^3\mathrm{He}}(\pi\hbar^2c^2)^3\gamma^2}{3\sqrt{3}\left[\frac{C}{2}R_f^2(\boldsymbol{p}) + \sigma_{^3\mathrm{He}}^2\right]\sqrt{\frac{C}{2}[R_f(\boldsymbol{p})/\gamma]^2 + \sigma_{^3\mathrm{He}}^2}} \frac{1}{\left[\frac{2C}{3}R_f^2(\boldsymbol{p}) + \sigma_{^3\mathrm{He}}^2\right]\sqrt{\frac{2C}{3}[R_f(\boldsymbol{p})/\gamma]^2 + \sigma_{^3\mathrm{He}}^2}} f_p\left(\frac{\boldsymbol{p}}{3}\right) f_p\left(\frac{\boldsymbol{p}}{3}\right) f_n\left(\frac{\boldsymbol{p}}{3}\right). \tag{23}$$

From Eqs. (22) and (23), we can get the Lorentz-invariant momentum distributions of light nuclei. We denote the invariant distribution $\frac{d^2N}{2\pi p_T dp_T dy}$ with $f^{(inv)}$ and at the midrapidity $y = 0$ we have

$$f_d^{(inv)}(p_T) = \frac{32g_d(\sqrt{\pi}\hbar c)^3}{m_d\left[CR_f^2(p_T) + \sigma_d^2\right]\sqrt{C[R_f(p_T)/\gamma]^2 + \sigma_d^2}} f_p^{(inv)}\left(\frac{p_T}{2}\right) f_n^{(inv)}\left(\frac{p_T}{2}\right), \tag{24}$$

$$f_{^3\mathrm{He}}^{(inv)}(p_T) = \frac{192\sqrt{3}g_{^3\mathrm{He}}(\pi\hbar^2c^2)^3}{m_{^3\mathrm{He}}^2\left[\frac{C}{2}R_f^2(p_T) + \sigma_{^3\mathrm{He}}^2\right]\left[\frac{2C}{3}R_f^2(p_T) + \sigma_{^3\mathrm{He}}^2\right]} \frac{1}{\sqrt{\frac{C}{2}[R_f(p_T)/\gamma]^2 + \sigma_{^3\mathrm{He}}^2}\sqrt{\frac{2C}{3}[R_f(p_T)/\gamma]^2 + \sigma_{^3\mathrm{He}}^2}} \times f_p^{(inv)}\left(\frac{p_T}{3}\right) f_p^{(inv)}\left(\frac{p_T}{3}\right) f_n^{(inv)}\left(\frac{p_T}{3}\right). \tag{25}$$

Here, m_d is the mass of the d and $m_{^3\mathrm{He}}$ is that of the ^{3}He. For tritons, we similarly have

$$f_t^{(inv)}(p_T) = \frac{192\sqrt{3}g_t(\pi\hbar^2c^2)^3}{m_t^2\left[\frac{C}{2}R_f^2(p_T) + \sigma_t^2\right]\left[\frac{2C}{3}R_f^2(p_T) + \sigma_t^2\right]} \frac{1}{\sqrt{\frac{C}{2}[R_f(p_T)/\gamma]^2 + \sigma_t^2}\sqrt{\frac{2C}{3}[R_f(p_T)/\gamma]^2 + \sigma_t^2}} \times f_p^{(inv)}\left(\frac{p_T}{3}\right) f_n^{(inv)}\left(\frac{p_T}{3}\right) f_n^{(inv)}\left(\frac{p_T}{3}\right), \tag{26}$$

where $g_t = 1/4$ and $\sigma_t = R_t = 1.7591$ fm [61]. m_t is the mass of the t. Equations (24)–(26) show relationships of light nuclei with primordial nucleons in momentum space in the laboratory frame. They can be used to calculate coalescence factors, yield rapidity densities and p_T spectra of light nuclei in high energy collisions, especially in heavy ion collisions at the LHC where the coupling effect of coordinate and momentum may be more intense due to stronger collective motions and larger temperature gradients. We will show their applications in Pb-Pb collisions at $\sqrt{s_{NN}} = 2.76$ TeV in the following sections. The d, ^{3}He, and t coming from decays of the excited nuclei are neglected in the current work, which have been estimated to be less than 5% at the LHC [69].

III. RESULTS OF COALESCENCE FACTORS

The coalescence factor B_A is defined as

$$B_A = f_{d,^3\mathrm{He},t}^{(inv)}(p_T)/\left[\left(f_p^{(inv)}\left(\frac{p_T}{A}\right)\right)^Z\left(f_n^{(inv)}\left(\frac{p_T}{A}\right)\right)^{A-Z}\right], \tag{27}$$

where A is the mass number and Z is the charge of the light nuclei. B_A is a key link between the formed light nuclei and the primordial nucleons, and folds important kinetic and dynamical information of the coalescence process. Intuitively unfolding B_A and a quantitative explanation for its centrality and p_T-dependent behaviors in heavy ion collisions at the LHC are necessary.

Substituting Eqs. (24)–(26) into Eq. (27), we respectively have, for d, ^{3}He, and t,

$$B_2(p_T) = \frac{32 g_d (\sqrt{\pi}\hbar c)^3}{m_d \left[C R_f^2(p_T) + \sigma_d^2\right] \sqrt{C[R_f(p_T)/\gamma]^2 + \sigma_d^2}}, \tag{28}$$

$$B_3(p_T) = \frac{192\sqrt{3} g_{^3\mathrm{He}} (\pi\hbar^2 c^2)^3}{m_{^3\mathrm{He}}^2 \left[\frac{C}{2} R_f^2(p_T) + \sigma_{^3\mathrm{He}}^2\right]\left[\frac{2C}{3} R_f^2(p_T) + \sigma_{^3\mathrm{He}}^2\right]} \frac{1}{\sqrt{\frac{C}{2}[R_f(p_T)/\gamma]^2 + \sigma_{^3\mathrm{He}}^2}\sqrt{\frac{2C}{3}[R_f(p_T)/\gamma]^2 + \sigma_{^3\mathrm{He}}^2}}, \tag{29}$$

$$B_3(p_T) = \frac{192\sqrt{3} g_t (\pi\hbar^2 c^2)^3}{m_t^2 \left[\frac{C}{2} R_f^2(p_T) + \sigma_t^2\right]\left[\frac{2C}{3} R_f^2(p_T) + \sigma_t^2\right]} \frac{1}{\sqrt{\frac{C}{2}[R_f(p_T)/\gamma]^2 + \sigma_t^2}\sqrt{\frac{2C}{3}[R_f(p_T)/\gamma]^2 + \sigma_t^2}}. \tag{30}$$

The above equations clearly show that B_2 and B_3 depend on the masses $m_{d,^3\mathrm{He},t}$, the spin degeneracy factors $g_{d,^3\mathrm{He},t}$ and the sizes of light nuclei via $\sigma_{d,^3\mathrm{He},t}$. The Lorentz contraction factor γ, resulting from setting nucleon coalescence criteria in the rest frame of the nucleon pair or three-nucleon cluster rather than in the laboratory frame, affects the p_T-dependent behaviors of B_2 and B_3. This has been studied in Ref. [55]. The other influencing factor for p_T-dependent behaviors of B_2 and B_3 is the $R_f(p_T)$, which is also closely related with centrality-dependent behaviors of B_2 and B_3.

To further compute B_2 and B_3, the specific form of $R_f(p_T)$ is necessary. In heavy ion collisions at CERN-SPS energies, it has been found that $R_f(p_T)$ adopted as the femtoscopic radius can describe the d production well [42]. If this still holds at LHC energies, the dependence of $R_f(p_T)$ on centrality and p_T should factorize into a linear dependence on the cube root of the pseudorapidity density of charged particles $(dN_{\mathrm{ch}}/d\eta)^{1/3}$ and a power-law dependence on the transverse mass of the formed light nucleus m_T [66]. So we get

$$R_f(p_T) = a \times \left(\frac{dN_{\mathrm{ch}}}{d\eta}\right)^{1/3} \times \left(\sqrt{p_T^2 + m_{d,^3\mathrm{He},t}^2}\right)^b, \tag{31}$$

where a and b are free parameters. Their values in Pb-Pb collisions at $\sqrt{s_{NN}} = 2.76$ TeV are (0.67,−0.25) for d and (0.60,−0.25) for ^{3}He and t, which are determined by reproducing the data of the p_T spectrum of d in 0–10% centrality and that of ^{3}He in 0–20% centrality. Note that $b < 0$ gives decreasing R_f with the increasing p_T. This means that nucleons with stronger collective motions have larger probability to emit from the same spatial location. Such coordinate-momentum correlation is naturally given by the gaussian form of the relative coordinate distribution in Eqs. (17) and (18). Here, b is set to be centrality independent, which is consistent with that in hydrodynamics [71] and that in STAR measurements of two-pion interferometry in central and semicentral Au-Au collisions [72]. a is also centrality independent. Precise experimental measurements of HBT femtoscopic radius for nucleons in the future can crosscheck the scaling behaviors of R_f as functions of $dN_{\mathrm{ch}}/d\eta$ and p_T.

We use the data of $dN_{\mathrm{ch}}/d\eta$ in Ref. [73] to get $R_f(p_T)$, and then compute B_2 and B_3. Figure 1 shows B_2 of d as a function of the transverse momentum scaled by the mass number $p_T/2$ in different centralities in Pb-Pb collisions at $\sqrt{s_{NN}} = 2.76$ TeV. Symbols with error bars are experimental data [18,70] and different solid lines are our theoretical results of the current nucleon coalescence model. Different dotted lines are results from Ref. [55] where the assumption of the coordinate-momentum factorization was adopted. From Fig. 1, one can see from central to peripheral collisions, B_2 increases. This is due to the decreasing scale of the hadronic system, which makes it easier for a pn pair to recombine into a deuteron. For the same centrality, B_2 increase as a function of $p_T/2$. This increase behavior results on one hand from the Lorentz contraction factor γ [55]. On the other hand, it results from the decreasing R_f with increasing momentum. The rising behavior of the experimental data as a function of $p_T/2$ from central to peripheral collisions can be

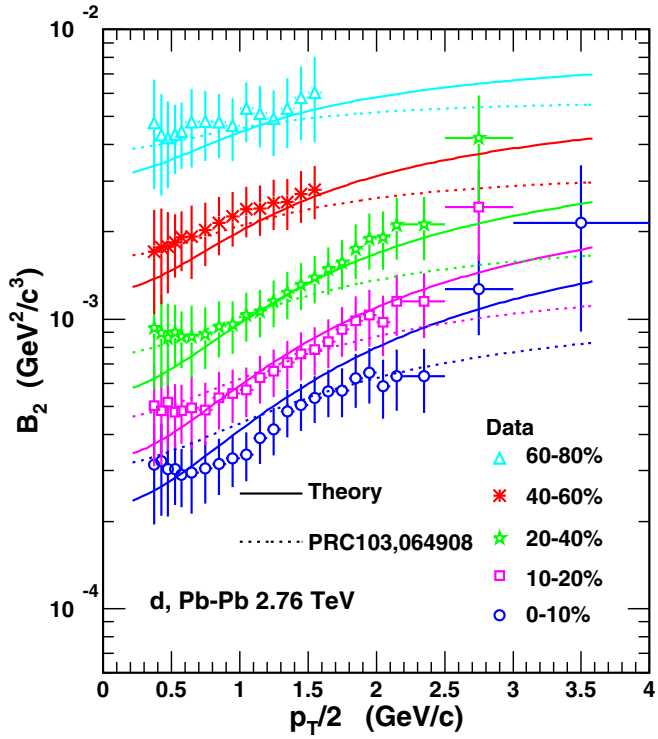

FIG. 1. The B_2 of d as a function of $p_T/2$ in different centralities in Pb-Pb collisions at $\sqrt{s_{NN}} = 2.76$ TeV. Symbols with error bars are experimental data [18,70] and different solid lines are theoretical results. Different dotted lines are results with the coordinate-momentum factorization assumption in Ref. [55].

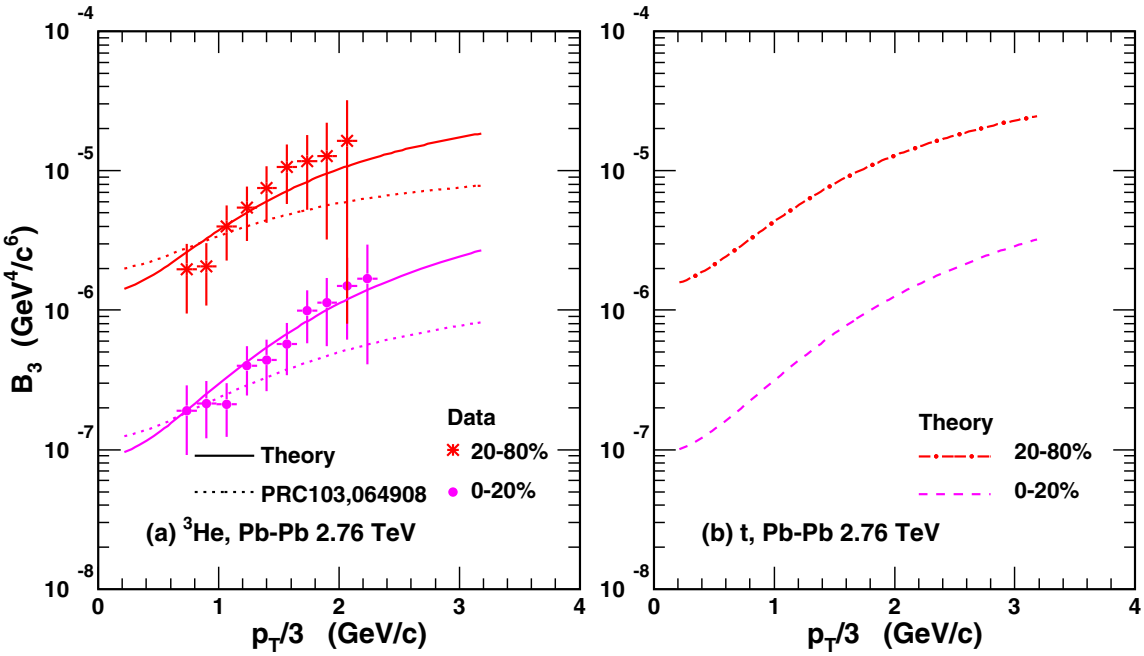

FIG. 2. The B_3 of (a) ^{3}He and (b) t as a function of $p_T/3$ in different centralities in Pb-Pb collisions at $\sqrt{s_{NN}} = 2.76$ TeV. Symbols with error bars are experimental data [18] and different solid, dashed, and dash-dotted lines are our theoretical results. Different dotted lines in (a) are results of ^{3}He with the coordinate-momentum factorization assumption in Ref. [55].

quantitatively described by the current nucleon coalescence model. Comparing the current results denoted by solid lines with those in Ref. [55] denoted by dotted lines in Fig. 1, one can see the nucleon coalescence model with the coordinate-momentum correlation can better describe the behaviors of B_2 in central and semicentral collisions. This shows the necessity of the coordinate-momentum correlation in large heavy ion collision systems. For low $p_T/2 < 1$ GeV area in peripheral collisions, the data seem to favor the coalescence model with the coordinate-momentum factorization assumption. Recalling that we fix the correlation strength parameter b with the experimental data in central collisions and set it to be centrality-independent, this indicates that the strength of the coordinate-momentum correlation may become weak due to the weak collective motion in peripheral collisions.

Figure 2(a) shows B_3 of ^{3}He as a function of $p_T/3$ in different centralities in Pb-Pb collisions at $\sqrt{s_{NN}} = 2.76$ TeV. Symbols with error bars are experimental data [18] and different solid lines are our theoretical results. Different dotted lines are results from Ref. [55] where the assumption of the coordinate-momentum factorization was adopted. Similarly as B_2, experimental data of B_3 for ^{3}He also exhibits a rising trend as a function of $p_T/3$, which is reproduced well by the current nucleon coalescence model from central to peripheral collisions. Predictions of B_3 for t in Fig. 2(b) show similar trend as that of ^{3}He, which can be tested by future experimental measurements. Compared the current results denoted by solid lines with those in Ref. [55] denoted by dotted lines in Fig. 2(a), one can see the improved nucleon coalescence model can describe the slopes of B_3 much better.

At the end of this section, we want to emphasize that the centrality and momentum dependent behaviors of B_2 and B_3 in Pb-Pb collisions at $\sqrt{s_{NN}} = 2.76$ TeV are simultaneously explained by the improved nucleon coalescence model. The influencing factors of B_2 and B_3 are explicitly unfolded, as shown in Eqs. (28)–(30). Some other models based on transport approach are also used to study behaviors of B_A in heavy ion collisions at LHC and other experiments [48,74–78]. All the results from these different models can help cross understand production properties of light nuclei from different aspects.

IV. RESULTS OF p_T SPECTRA

In this section, we use the nucleon coalescence model to study the p_T spectra of light nuclei in different centralities in Pb-Pb collisions at $\sqrt{s_{NN}} = 2.76$ TeV. We first introduce the nucleon p_T spectra. We then compute the p_T spectra of d, ^{3}He and t. We finally calculate the averaged transverse momenta $\langle p_T \rangle$, the yield rapidity densities dN/dy, and yield ratios of different light nuclei.

A. The p_T spectra of primordial nucleons

The p_T spectra of primordial nucleons are necessary inputs for computing p_T distributions of light nuclei in the nucleon coalescence model. We here use the blast-wave model to get p_T distribution functions of primordial protons by fitting the experimental data of prompt (anti)protons in Ref. [73]. The blast-wave function [79] is given as

$$\frac{d^2N}{2\pi p_T dp_T dy} \propto \int_0^R r dr m_T I_0\left(\frac{p_T \sinh\rho}{T_{kin}}\right) K_1\left(\frac{m_T \cosh\rho}{T_{kin}}\right), \tag{32}$$

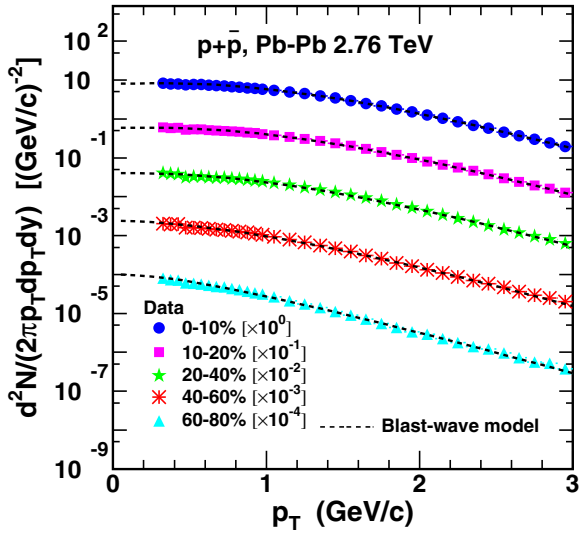

FIG. 3. The p_T spectra of prompt protons plus antiprotons in different centralities in Pb-Pb collisions at $\sqrt{s_{NN}} = 2.76$ TeV. Symbols with error bars are experimental data [73], and different lines are the results of the blast-wave model.

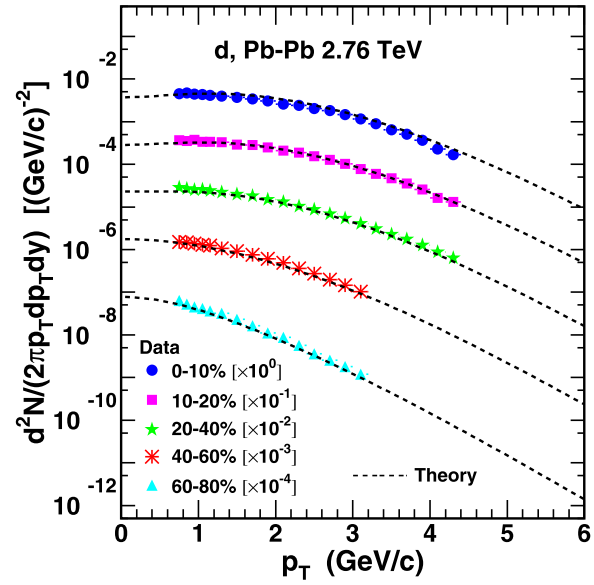

FIG. 4. The p_T spectra of deuterons in different centralities in Pb-Pb collisions at $\sqrt{s_{NN}} = 2.76$ TeV. Symbols are experimental data [18] and different lines are the theoretical results.

where r is the radial distance in the transverse plane and R is the radius of the fireball. m_T is the transverse mass of the proton. I_0 and K_1 are the modified Bessel functions, and the velocity profile $\rho = \tanh^{-1}[\beta_s(\frac{r}{R})^n]$. The surface velocity β_s, the kinetic freeze-out temperature T_{kin} and n are fitting parameters.

Figure 3 shows the p_T spectra of prompt protons plus antiprotons in different centralities in Pb-Pb collisions at $\sqrt{s_{NN}} = 2.76$ TeV. Symbols with error bars are experimental data [73], and different lines are the results of the blast-wave model. The p_T spectra in different centralities are scaled by different factors for clarity as shown in the figure. For the primordial neutron p_T spectra, we adopt the same as those of primordial protons as we focus on light nuclei production at midrapidity at so high LHC energy that the isospin symmetry is well satisfied. We, in the following, use these nucleon results from the blast-wave model to compute the productions of different light nuclei.

B. The p_T spectra of light nuclei

With Eq. (24), we first calculate the p_T spectra of deuterons in Pb-Pb collisions at $\sqrt{s_{NN}} = 2.76$ TeV in 0–10%, 10–20%, 20–40%, 40–60%, and 60–80% centralities. Different lines scaled by different factors for clarity in Fig. 4 are our theoretical results. Symbols with error bars are experimental data from the ALICE collaboration [18]. From Fig. 4, one can see the $p + n$ coalescence can well reproduce the available data from central to peripheral Pb-Pb collisions at $\sqrt{s_{NN}} = 2.76$ TeV.

We then study the p_T spectra of ^{3}He and t in Pb-Pb collisions at $\sqrt{s_{NN}} = 2.76$ TeV in 0–20% and 20–80% centralities. Different lines in Fig. 5(a) are our theoretical results of ^{3}He, which agree with the available data denoted by filled symbols [18] within experimental uncertainties. In the low $p_T < 2\,\mathrm{GeV}/c$ region where the data are absent, our theoretical results show different trends in different centralities, slight increase in 0–20% centrality but decrease in 20–80% centrality. This difference is caused by the competition of the p_T distributions of nucleons and $R_f(p_T)$ in our model. With the increase of the p_T, the decreasing nucleon p_T distributions suppress ^{3}He production while decreasing $R_f(p_T)$ enhances its production. In central 0–20% collisions, nucleon p_T distributions decrease very weakly or nearly hold invariant in $p_T < 0.6\,\mathrm{GeV}/c$, so decreasing $R_f(p_T)$ as the function of p_T makes the p_T spectra of ^{3}He increase in $p_T < 2\,\mathrm{GeV}/c$. In 20–80% centrality, although decreasing $R_f(p_T)$ still makes the p_T spectra of ^{3}He increase as the function of p_T, but obvious decreasing p_T distributions of nucleons in $p_T < 0.6\,\mathrm{GeV}/c$ dominate the decreasing behavior of the p_T spectra of ^{3}He. Future experimental measurements at low p_T area can test the pattern of the $R_f(p_T)$ and the coalescence production mechanism for ^{3}He. The dashed and dash-dotted lines in Fig. 5(b) are predictions for t in centralities 0–20% and 20–80%, respectively.

C. Averaged transverse momenta and yield rapidity densities of light nuclei

We here study the averaged transverse momenta $\langle p_T \rangle$ and yield rapidity densities dN/dy of d, ^{3}He, and t. Our theoretical results are put in the fourth and sixth columns in Table I. Experimental data in the third and fifth columns are from Ref. [18]. Theoretical results for d and ^{3}He are consistent with the corresponding data within the experimental uncertainties. Predictions for t are provided for future experimental measurements. A clear decreasing trend for both $\langle p_T \rangle$ and dN/dy from central to peripheral collisions is observed. This is due to that in more central collisions more energy is deposited in the midrapidity region and collective evolution exists longer.

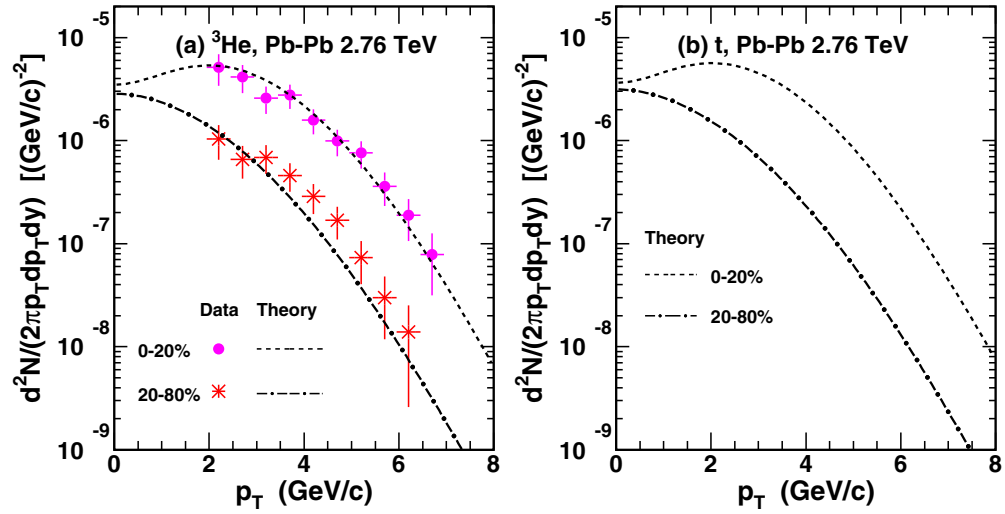

FIG. 5. The p_T spectra of (a) ^{3}He and (b) t in different centralities in Pb-Pb collisions at $\sqrt{s_{NN}} = 2.76$ TeV. Symbols are experimental data [18] and different lines are the theoretical results.

D. Yield ratios of light nuclei

Yield ratios of light nuclei are characteristic probes for production mechanisms and contain intrinsic production correlations among different light nuclei. In this subsection, we study three groups of yield ratios. One is two-particle ratios such as d/p, ^{3}He$/d$, t/p, and ^{3}He$/p$. The second group includes d/p^2 and ^{3}He$/p^3$. They represent the probability of any nucleon-pair coalescing into a d and that of any ppn cluster coalescing into a ^{3}He. The last is $t/^3$He, which exhibits interesting behaviors as functions of p_T and the collision centrality.

From Eqs. (24)–(26) we approximately have the p_T-integrated yield ratios

$$\frac{d}{p} \propto \frac{N_p}{\langle R_f\rangle^3\left(C+\frac{\sigma_d^2}{\langle R_f\rangle^2}\right)\sqrt{\frac{C}{\langle\gamma\rangle^2}+\frac{\sigma_d^2}{\langle R_f\rangle^2}}} = \frac{N_p}{\frac{\langle R_f\rangle^3}{\langle\gamma\rangle}\left(C+\frac{\sigma_d^2}{\langle R_f\rangle^2}\right)\sqrt{C+\frac{\sigma_d^2}{\langle R_f\rangle^2/\langle\gamma\rangle^2}}}, \tag{33}$$

$$\begin{aligned}\frac{^3\text{He}}{d} &\propto \frac{N_p\left(C+\frac{\sigma_d^2}{\langle R_f\rangle^2}\right)\sqrt{\frac{C}{\langle\gamma\rangle^2}+\frac{\sigma_d^2}{\langle R_f\rangle^2}}}{\langle R_f\rangle^3\left(\frac{C}{2}+\frac{\sigma_{^3\text{He}}^2}{\langle R_f\rangle^2}\right)\sqrt{\frac{C}{2\langle\gamma\rangle^2}+\frac{\sigma_{^3\text{He}}^2}{\langle R_f\rangle^2}}} \\ &\times \frac{1}{\left(\frac{2C}{3}+\frac{\sigma_{^3\text{He}}^2}{\langle R_f\rangle^2}\right)\sqrt{\frac{2C}{3\langle\gamma\rangle^2}+\frac{\sigma_{^3\text{He}}^2}{\langle R_f\rangle^2}}} \\ &\approx \frac{2^{3/2}N_p}{\langle R_f\rangle^3\left(\frac{2C}{3}+\frac{\sigma_{^3\text{He}}^2}{\langle R_f\rangle^2}\right)\sqrt{\frac{2C}{3\langle\gamma\rangle^2}+\frac{\sigma_{^3\text{He}}^2}{\langle R_f\rangle^2}}} \\ &\times\left\{1+\Delta\epsilon^2\left[\frac{1}{1+\frac{C\langle R_f\rangle^2}{(\sqrt{2}\sigma_{^3\text{He}})^2}}+\frac{1/2}{1+\frac{C\langle R_f\rangle^2/\langle\gamma\rangle^2}{(\sqrt{2}\sigma_{^3\text{He}})^2}}\right]\right\},\end{aligned} \tag{34}$$

$$\frac{t}{p} \propto \frac{N_p^2}{\langle R_f\rangle^6\left(\frac{C}{2}+\frac{\sigma_t^2}{\langle R_f\rangle^2}\right)\left(\frac{2C}{3}+\frac{\sigma_t^2}{\langle R_f\rangle^2}\right)} \times \frac{1}{\sqrt{\frac{C}{2\langle\gamma\rangle^2}+\frac{\sigma_t^2}{\langle R_f\rangle^2}}\sqrt{\frac{2C}{3\langle\gamma\rangle^2}+\frac{\sigma_t^2}{\langle R_f\rangle^2}}}, \tag{35}$$

TABLE I. Averaged transverse momenta $\langle p_T\rangle$ and yield rapidity densities dN/dy of d, ^{3}He, and t in different centralities in Pb-Pb collisions at $\sqrt{s_{NN}} = 2.76$ TeV. Experimental data in the third and fifth columns are from Ref. [18]. Theoretical results are in the fourth and sixth columns.

		$\langle p_T\rangle$		dN/dy	
	Centrality	Data	Theory	Data	Theory
d	0–10%	$2.12 \pm 0.00 \pm 0.09$	2.19	$(9.82 \pm 0.04 \pm 1.58) \times 10^{-2}$	11.38×10^{-2}
	10–20%	$2.07 \pm 0.01 \pm 0.10$	2.12	$(7.60 \pm 0.04 \pm 1.25) \times 10^{-2}$	7.55×10^{-2}
	20–40%	$1.92 \pm 0.00 \pm 0.11$	1.95	$(4.76 \pm 0.02 \pm 0.82) \times 10^{-2}$	4.28×10^{-2}
	40–60%	$1.63 \pm 0.01 \pm 0.09$	1.62	$(1.90 \pm 0.01 \pm 0.41) \times 10^{-2}$	1.71×10^{-2}
	60–80%	$1.29 \pm 0.01 \pm 0.14$	1.28	$(0.51 \pm 0.01 \pm 0.14) \times 10^{-2}$	0.42×10^{-2}
^{3}He	0–20%	$2.83 \pm 0.05 \pm 0.45$	2.95	$(2.76 \pm 0.09 \pm 0.62) \times 10^{-4}$	2.60×10^{-4}
	20–80%	$2.65 \pm 0.06 \pm 0.45$	2.18	$(5.09 \pm 0.24 \pm 1.36) \times 10^{-5}$	5.14×10^{-5}
t	0–20%	– – –	2.97	– – –	2.77×10^{-4}
	20–80%	– – –	2.20	– – –	5.84×10^{-5}

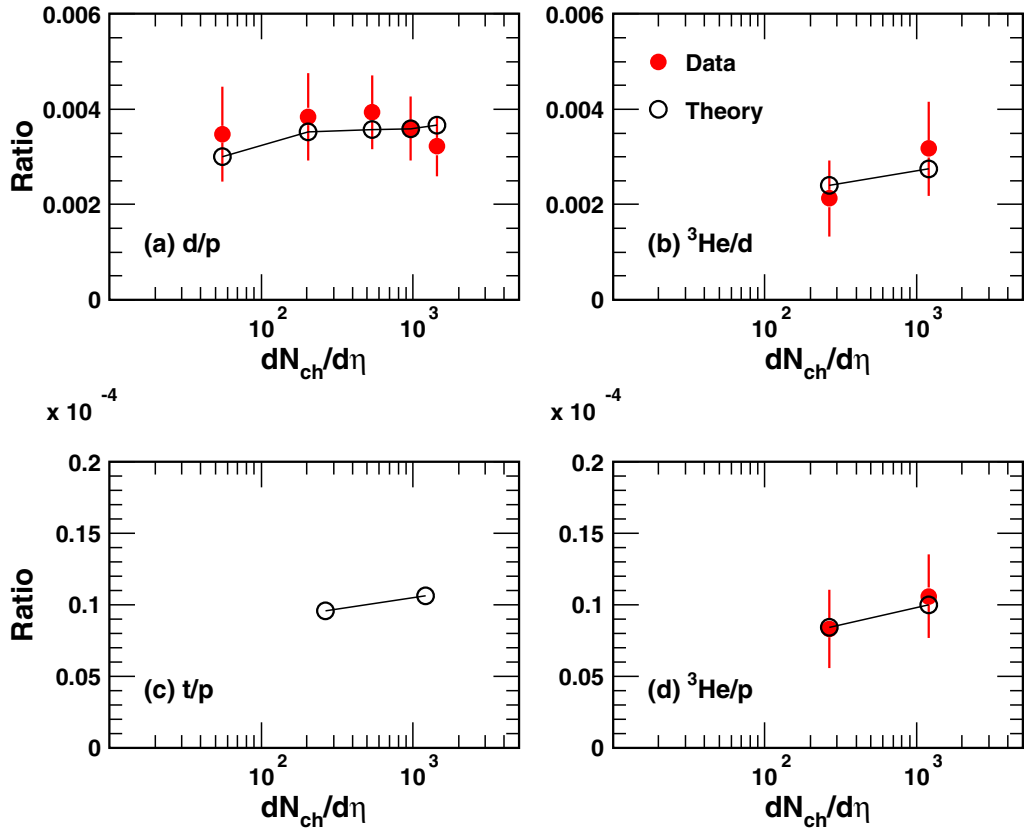

FIG. 6. Yield ratios (a) d/p, (b) ^{3}He $/d$, (c) t/p, and (d) ^{3}He $/p$ as a function of $dN_{\rm ch}/d\eta$ in Pb-Pb collisions at $\sqrt{s_{NN}} = 2.76$ TeV. Filled circles are experimental data [18] and open circles connected with solid lines to guide the eye are the theoretical results.

$$\frac{^3\mathrm{He}}{p} \propto \frac{N_p^2}{\langle R_f\rangle^6\left(\frac{C}{2}+\frac{\sigma^2_{^3\mathrm{He}}}{\langle R_f\rangle^2}\right)\left(\frac{2C}{3}+\frac{\sigma^2_{^3\mathrm{He}}}{\langle R_f\rangle^2}\right)} \times \frac{1}{\sqrt{\frac{C}{2\langle\gamma\rangle^2}+\frac{\sigma^2_{^3\mathrm{He}}}{\langle R_f\rangle^2}}\sqrt{\frac{2C}{3\langle\gamma\rangle^2}+\frac{\sigma^2_{^3\mathrm{He}}}{\langle R_f\rangle^2}}}. \tag{36}$$

The angle brackets denote the averaged values. Note that in the approximately equal sign in Eq. (34), we ignore the difference of $\langle R_f\rangle$ and that of $\langle\gamma\rangle$ for d and ^{3}He and ignore the higher order terms of $\Delta\epsilon^2$, where $\Delta\epsilon^2 = [\sigma_d^2 - (\sqrt{2}\sigma_{^3\mathrm{He}})^2]/(\sqrt{2}\sigma_{^3\mathrm{He}})^2 < 1$. Equations (33)–(36) show that centrality-dependent behaviors of these two-particle ratios are closely related with the nucleon density $N_p/\langle R_f\rangle^3$, $\sigma_d/\langle R_f\rangle$ and $\langle\gamma\rangle$. From peripheral to central collisions, i.e., with the increasing $dN_{\rm ch}/d\eta$, $\langle R_f\rangle$, and $\langle\gamma\rangle$ increase. Suppressions on these ratios from $\sigma_{d,^3\mathrm{He},t}/\langle R_f\rangle$ and $1/\langle\gamma\rangle^2$ become weak, and this makes these ratios increase. The nucleon density $N_p/\langle R_f\rangle^3$ decreases with increasing $dN_{\rm ch}/d\eta$, which can be deduced from the trend of the yield ratio p/π [73]. This leads to the decrease of these ratios. The final behaviors of d/p, ^{3}He $/d$, t/p, and ^{3}He $/p$ as the function of the centrality dependence denoted by $dN_{\rm ch}/d\eta$ depend on the competition effect from $\sigma_{d,^3\mathrm{He},t}/\langle R_f\rangle$, $1/\langle\gamma\rangle^2$ and $N_p/\langle R_f\rangle^3$.

Figure 6 shows the $dN_{\rm ch}/d\eta$ dependence of d/p, ^{3}He $/d$, t/p, and ^{3}He $/p$ in Pb-Pb collisions at $\sqrt{s_{NN}} = 2.76$ TeV. Filled circles are experimental data [18]. Open circles connected with solid lines to guide the eye are our theoretical results. Results of our model agree with the available data within the experimental uncertainties. Equation (33) shows that d/p mainly relates to two elements. One is the nucleon volume density, i.e., $N_p/\frac{\langle R_f\rangle^3}{\langle\gamma\rangle}$. The other is the suppression effect due to the d size via σ_d, and this production suppression is weaker in larger reaction system due to the item $\sigma_d/\langle R_f\rangle$. Therefore, in more central collisions weaker suppression effect from $\sigma_d/\langle R_f\rangle$ makes d/p increase, but the observed decreasing proton density [73] makes d/p decrease. The finally conjunct result from the nucleon volume density and the suppression effect due to the d size makes d/p unchanged within the experimental errors as the function of the collision centrality, as shown in Fig. 6(a). In Ref. [80], a small drop of d/p from the proton suppression production in central Pb-Pb collisions at LHC has also been studied. Figures 6(b), 6(c), and 6(d) show ^{3}He $/d$, t/p, and ^{3}He $/p$ increase slightly as the function of $dN_{\rm ch}/d\eta$. The large experimental uncertainties of the data [18] make it hard to give a final conclusion. The canonical effect in the thermal model leading to a reduction in peripheral collisions and the baryon-antibaryon annihilations in the hybrid simulation leading to an additional suppression in central collisions for d/p and ^{3}He $/p$ have been discussed in Ref. [81]. Discussions from different models give explanations of these ratios from different viewpoints.

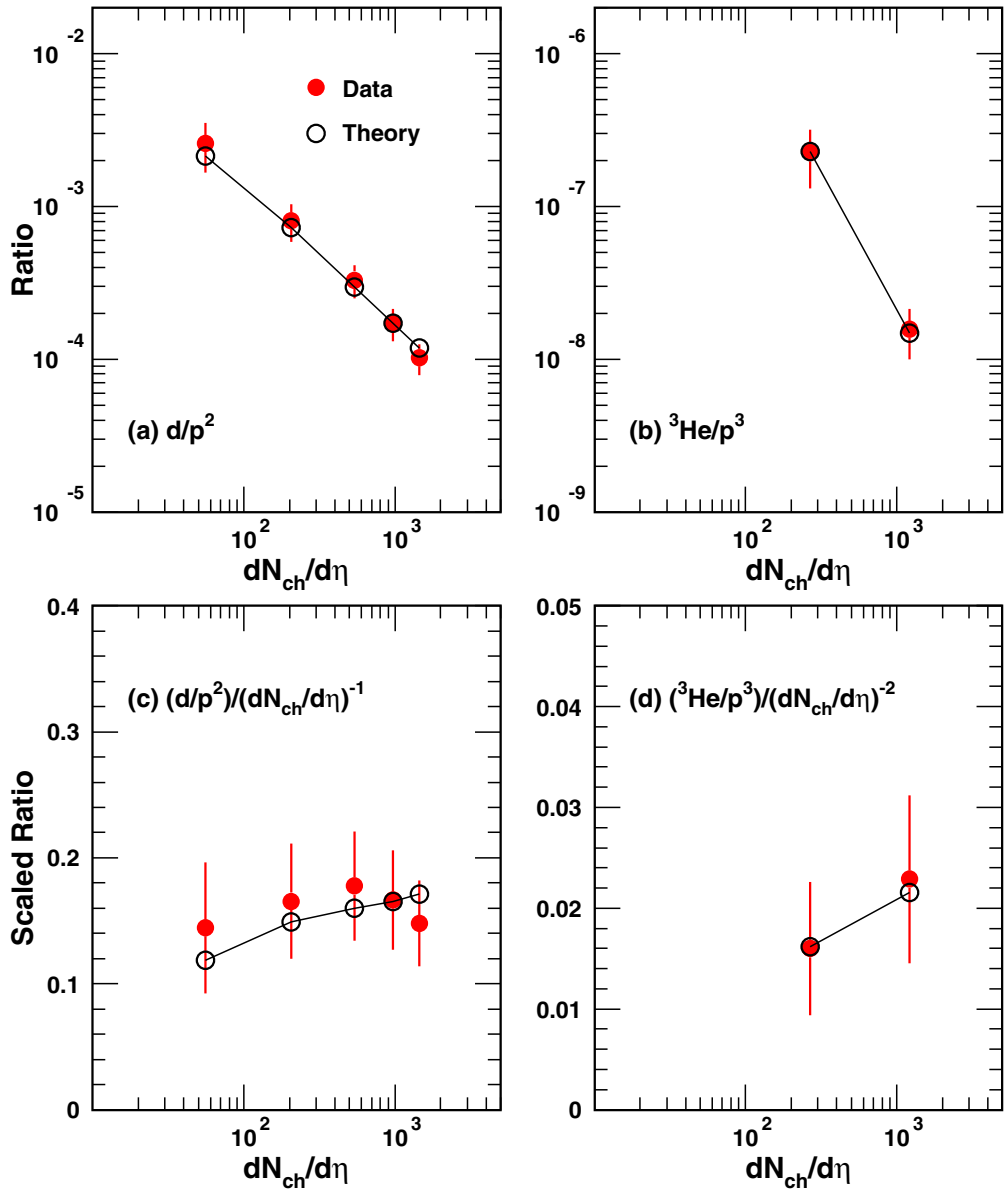

FIG. 7. Yield ratios (a) d/p^2 and (b) $^3\mathrm{He}/p^3$ as well as scaled yield ratios (c) $(d/p^2)/(dN_{\mathrm{ch}}/d\eta)^{-1}$ and (d) $(^3\mathrm{He}/p^3)/(\mathrm{dN_{ch}}/d\eta)^{-2}$ as a function of $dN_{\mathrm{ch}}/d\eta$ in Pb-Pb collisions at $\sqrt{s_{NN}} = 2.76$ TeV. Filled circles are experimental data [18] and open circles connected with solid lines to guide the eye are the theoretical results.

From Eqs. (33) and (36), we immediately have

$$\frac{d}{p^2} \propto \frac{1}{\langle R_f\rangle^3\left(C+\frac{\sigma_d^2}{\langle R_f\rangle^2}\right)\sqrt{\frac{C}{\langle\gamma\rangle^2}+\frac{\sigma_d^2}{\langle R_f\rangle^2}}}, \tag{37}$$

$$\frac{^3\mathrm{He}}{p^3} \propto \frac{1}{\langle R_f\rangle^6\left(\frac{C}{2}+\frac{\sigma_{^3\mathrm{He}}^2}{\langle R_f\rangle^2}\right)\left(\frac{2C}{3}+\frac{\sigma_{^3\mathrm{He}}^2}{\langle R_f\rangle^2}\right)} \times \frac{1}{\sqrt{\frac{C}{2\langle\gamma\rangle^2}+\frac{\sigma_{^3\mathrm{He}}^2}{\langle R_f\rangle^2}}\sqrt{\frac{2C}{3\langle\gamma\rangle^2}+\frac{\sigma_{^3\mathrm{He}}^2}{\langle R_f\rangle^2}}}. \tag{38}$$

They give a decreasing trend with the increasing R_f. They do not depend on the absolute nucleon numbers or the nucleon rapidity densities. Figures 7(a) and 7(b) show the ratios d/p^2 and $^3\mathrm{He}/p^3$, respectively, in Pb-Pb collisions at $\sqrt{s_{NN}} = 2.76$ TeV. Both d/p^2 and $^3\mathrm{He}/p^3$ show explicit decreasing trend with the increasing $dN_{\mathrm{ch}}/d\eta$, which is very different from the previous d/p and $^3\mathrm{He}/p$. Recalling that d/p^2 and $^3\mathrm{He}/p^3$ represent the probability of any nucleon-pair coalescing into a deuteron and that of any ppn-cluster coalescing into a ^{3}He. This means that it is more difficult for any nucleon pair or ppn cluster to recombine into a deuteron or ^{3}He in larger hadronic system produced in more central collisions. Equations (37) and (38) approximately show an antiproportional relation between d/p^2 and $\langle R_f\rangle^3$ and that between $^3\mathrm{He}/p^3$ and $\langle R_f\rangle^6$. As $dN_{\mathrm{ch}}/d\eta$ is always regarded as a proxy of the system volume, i.e., $\langle R_f\rangle^3$, we have plotted the result of

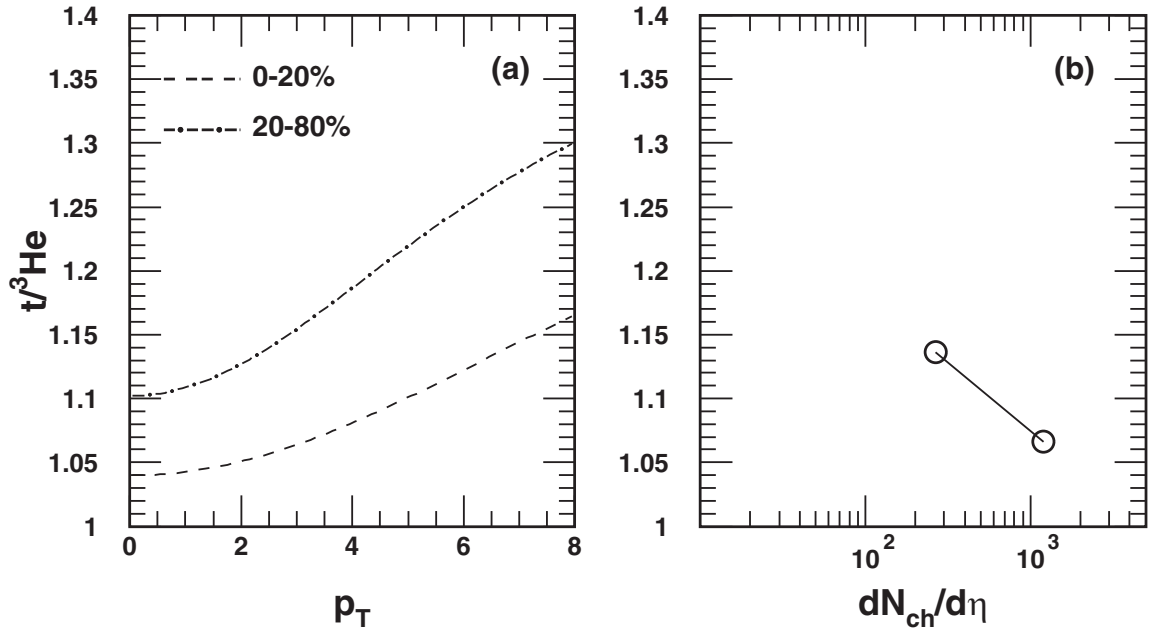

FIG. 8. Predictions of the yield ratio $t/{}^3\mathrm{He}$ as functions of (a) p_T and (b) $dN_{\mathrm{ch}}/d\eta$ in Pb-Pb collisions at $\sqrt{s_{NN}} = 2.76\,\mathrm{TeV}$.

d/p^2 divided by $(dN_{\mathrm{ch}}/d\eta)^{-1}$ and that of ${}^3\mathrm{He}/p^3$ divided by $(dN_{\mathrm{ch}}/d\eta)^{-2}$ as a function of $dN_{\mathrm{ch}}/d\eta$ in Fig. 7(c) and 7(d). The slight increase behaviors of the theoretical results for these scaled ratios are due to the weaker production suppression from the nuclei own sizes in larger hadronic systems, as shown by items in parentheses and square roots in Eqs. (37) and (38). Precise data at future experiments can help justify the nonconstant behaviors of these scaled ratios as the function of the collision centrality.

The yield ratio $t/{}^3\mathrm{He}$ provides another test of the coalescence productions for light nuclei. With Eqs. (25) and (26), we have its p_T-dependent function as

$$\begin{aligned}\frac{t}{{}^3\mathrm{He}}(p_T) &= \frac{\left[\frac{C}{2}+\frac{\sigma^2_{{}^3\mathrm{He}}}{R_f^2(p_T)}\right]\left[\frac{2C}{3}+\frac{\sigma^2_{{}^3\mathrm{He}}}{R_f^2(p_T)}\right]}{\left[\frac{C}{2}+\frac{\sigma_t^2}{R_f^2(p_T)}\right]\left[\frac{2C}{3}+\frac{\sigma_t^2}{R_f^2(p_T)}\right]} \\ &\times \frac{\sqrt{\frac{C}{2\gamma^2}+\frac{\sigma^2_{{}^3\mathrm{He}}}{R_f^2(p_T)}}\sqrt{\frac{2C}{3\gamma^2}+\frac{\sigma^2_{{}^3\mathrm{He}}}{R_f^2(p_T)}}}{\sqrt{\frac{C}{2\gamma^2}+\frac{\sigma_t^2}{R_f^2(p_T)}}\sqrt{\frac{2C}{3\gamma^2}+\frac{\sigma_t^2}{R_f^2(p_T)}}} \\ &\approx 1+\frac{\Delta\sigma^2}{\sigma_t^2}\left\{\frac{1}{1+\frac{C}{2\sigma_t^2}R_f^2(p_T)}+\frac{1}{1+\frac{2C}{3\sigma_t^2}R_f^2(p_T)}\right. \\ &\left.+\frac{1/2}{1+\frac{C}{2\sigma_t^2\gamma^2}R_f^2(p_T)}+\frac{1/2}{1+\frac{2C}{3\sigma_t^2\gamma^2}R_f^2(p_T)}\right\}. \quad (39)\end{aligned}$$

Here, $\Delta\sigma^2 = \sigma^2_{{}^3\mathrm{He}} - \sigma_t^2$ and we ignore the higher order terms for the small quantity $\Delta\sigma^2/\sigma_t^2$. Eq. (39) shows that $t/{}^3\mathrm{He}$ is always larger than one and approaches to one when $R_f \to \infty$. The smaller R_f, the higher deviation of $t/{}^3\mathrm{He}$ from one. With the increasing p_T, γ increases and R_f decreases, so $t/{}^3\mathrm{He}$ should increase. Figure 8(a) shows our predictions of $t/{}^3\mathrm{He}$ as the function of p_T in 0–20% and 20–80% centralities, respectively, in Pb-Pb collisions at $\sqrt{s_{NN}} = 2.76\,\mathrm{TeV}$, both of which give increasing behaviors. The p_T-integrated yield ratio $t/{}^3\mathrm{He}$ as the function of $dN_{\mathrm{ch}}/d\eta$ is in Fig. 8(b), which has a decreasing trend. This is because larger $dN_{\mathrm{ch}}/d\eta$, i.e., larger R_f, makes $t/{}^3\mathrm{He}$ decrease closer to one. Predictions of $t/{}^3\mathrm{He}$ in the nucleon coalescence model give nonflat behaviors as functions of p_T and $dN_{\mathrm{ch}}/d\eta$. This is due to different relative production suppression between ${}^3\mathrm{He}$ and t at different hadronic system scales. This feature is very different from that in the thermal model, where the expectation for this ratio is one [30]. This can be used to distinguish production mechanisms of ${}^3\mathrm{He}$ and t.

V. SUMMARY

To get intuitive understandings of production properties of light nuclei in heavy ion collisions at the LHC, we improved a nucleon coalescence model analytically to include the coordinate-momentum correlation in nucleon joint distributions. We derived the momentum distributions of d, ${}^3\mathrm{He}$, and t. We obtained relationships of light nuclei with primordial nucleons in momentum space in the laboratory frame. We gave formulas of coalescence factors B_2, B_3, and yield ratios d/p, ${}^3\mathrm{He}/d$, t/p, ${}^3\mathrm{He}/p$, d/p^2, ${}^3\mathrm{He}/p^3$, $t/{}^3\mathrm{He}$.

We applied the improved nucleon coalescence model to Pb-Pb collisions at $\sqrt{s_{NN}} = 2.76\,\mathrm{TeV}$ to study productions of different light nuclei. We first investigated B_2 and B_3 and gave quantitative explanations for their interesting behaviors as functions of the collision centrality and the p_T/A. We then studied the centrality dependence of the p_T spectra, yield rapidity densities and averaged transverse momenta of d, ${}^3\mathrm{He}$, and t with the p_T distributions of kinetic freeze-out protons obtained from the blast-wave model. We finally studied yield ratios d/p, ${}^3\mathrm{He}/d$, t/p, ${}^3\mathrm{He}/p$, d/p^2, ${}^3\mathrm{He}/p^3$, $t/{}^3\mathrm{He}$ and discussed their behaviors as functions of the collision

centrality and the p_T. We found the nucleon coalescence model including the coordinate-momentum correlation can reproduce the experimental data available well. We furthermore found the system effective radius obtained in the coalescence production of light nuclei exhibited similar behaviors to HBT interferometry radius. We especially argued that nontrivial behaviors of yield ratios were valuable probes of production mechanisms of light nuclei.

ACKNOWLEDGMENTS

This work was supported in part by the National Natural Science Foundation of China under Grants No. 12175115 and 12375074, the Natural Science Foundation of Shandong Province, China, under Grant No. ZR2020MA097, and Higher Educational Youth Innovation Science and Technology Program of Shandong Province under Grant No. 2020KJJ004.

[1] J. L. Nagle, B. S. Kumar, M. J. Bennett, G. E. Diebold, J. K. Pope, H. Sorge, and J. P. Sullivan, Phys. Rev. Lett. **73**, 1219 (1994).
[2] J. Chen, D. Keane, Y.-G. Ma, A. Tang, and Z. Xu, Phys. Rep. **760**, 1 (2018).
[3] K. Blum and M. Takimoto, Phys. Rev. C **99**, 044913 (2019).
[4] S. Bazak and S. Mrowczynski, Eur. Phys. J. A **56**, 193 (2020).
[5] H. H. Gutbrod, A. Sandoval, P. J. Johansen, A. M. Poskanzer, J. Gosset, W. G. Meyer, G. D. Westfall, and R. Stock, Phys. Rev. Lett. **37**, 667 (1976).
[6] J. Aichelin, Phys. Rept. **202**, 233 (1991).
[7] A. Andronic, P. Braun-Munzinger, K. Redlich, and J. Stachel, Nature (London) **561**, 321 (2018).
[8] A. Bzdak, S. Esumi, V. Koch, J. Liao, M. Stephanov, and N. Xu, Phys. Rep. **853**, 1 (2020).
[9] K.-J. Sun, L.-W. Chen, C. M. Ko, and Z. Xu, Phys. Lett. B **774**, 103 (2017).
[10] K.-J. Sun, L.-W. Chen, C. M. Ko, J. Pu, and Z. Xu, Phys. Lett. B **781**, 499 (2018).
[11] X. Luo, S. Shi, N. Xu, and Y. Zhang, Particles **3**, 278 (2020).
[12] P. Junnarkar and N. Mathur, Phys. Rev. Lett. **123**, 162003 (2019).
[13] K. Morita, S. Gongyo, T. Hatsuda, T. Hyodo, Y. Kamiya, and A. Ohnishi, Phys. Rev. C **101**, 015201 (2020).
[14] C. Adler *et al.* (STAR Collaboration), Phys. Rev. Lett. **87**, 262301 (2001); **87**, 279902(E) (2001).
[15] S. Afanasiev *et al.* (PHENIX Collaboration), Phys. Rev. Lett. **99**, 052301 (2007).
[16] T. Anticic *et al.* (NA49 Collaboration), Phys. Rev. C **94**, 044906 (2016).
[17] S. Albergo *et al.*, Phys. Rev. C **65**, 034907 (2002).
[18] J. Adam *et al.* (ALICE Collaboration), Phys. Rev. C **93**, 024917 (2016).
[19] S. Acharya *et al.* (ALICE Collaboration), Phys. Rev. C **102**, 055203 (2020).
[20] L. Adamczyk *et al.* (STAR Collaboration), Phys. Rev. C **94**, 034908 (2016).
[21] J. Adam *et al.* (STAR Collaboration), Phys. Rev. C **102**, 044906 (2020).
[22] D. Zhang (STAR Collaboration), Nucl. Phys. A **1005**, 121825 (2021).
[23] J. Adam *et al.* (STAR Collaboration), Phys. Rev. C **99**, 064905 (2019).
[24] M. Abdulhamid *et al.* (STAR Collaboration), Phys. Rev. Lett. **130**, 202301 (2023).
[25] P. Braun-Munzinger and B. Dönigus, Nucl. Phys. A **987**, 144 (2019).
[26] D. Oliinychenko, Nucl. Phys. A **1005**, 121754 (2021).
[27] C. B. Dover, U. W. Heinz, E. Schnedermann, and J. Zimanyi, Phys. Rev. C **44**, 1636 (1991).
[28] L.-W. Chen, C. M. Ko, and B.-A. Li, Phys. Rev. C **68**, 017601 (2003).
[29] S. Mrowczynski, Eur. Phys. J.: Spec. Top. **229**, 3559 (2020).
[30] A. Andronic, P. Braun-Munzinger, J. Stachel, and H. Stocker, Phys. Lett. B **697**, 203 (2011).
[31] B. Dönigus, G. Röpke, and D. Blaschke, Phys. Rev. C **106**, 044908 (2022).
[32] A. Mekjian, Phys. Rev. Lett. **38**, 640 (1977).
[33] P. J. Siemens and J. I. Kapusta, Phys. Rev. Lett. **43**, 1486 (1979).
[34] J. Cleymans, S. Kabana, I. Kraus, H. Oeschler, K. Redlich, and N. Sharma, Phys. Rev. C **84**, 054916 (2011).
[35] Y. Cai, T. D. Cohen, B. A. Gelman, and Y. Yamauchi, Phys. Rev. C **100**, 024911 (2019).
[36] A. Schwarzschild and C. Zupancic, Phys. Rev. **129**, 854 (1963).
[37] H. Sato and K. Yazaki, Phys. Lett. B **98**, 153 (1981).
[38] R. Mattiello, A. Jahns, H. Sorge, H. Stocker, and W. Greiner, Phys. Rev. Lett. **74**, 2180 (1995).
[39] J. L. Nagle, B. S. Kumar, D. Kusnezov, H. Sorge, and R. Mattiello, Phys. Rev. C **53**, 367 (1996).
[40] R. Mattiello, H. Sorge, H. Stocker, and W. Greiner, Phys. Rev. C **55**, 1443 (1997).
[41] A. Polleri, J. P. Bondorf, and I. N. Mishustin, Phys. Lett. B **419**, 19 (1998).
[42] R. Scheibl and U. W. Heinz, Phys. Rev. C **59**, 1585 (1999).
[43] N. Sharma, T. Perez, A. Castro, L. Kumar, and C. Nattrass, Phys. Rev. C **98**, 014914 (2018).
[44] S. Bazak and S. Mrowczynski, Mod. Phys. Lett. A **33**, 1850142 (2018).
[45] W. Zhao, L. Zhu, H. Zheng, C. M. Ko, and H. Song, Phys. Rev. C **98**, 054905 (2018).
[46] P. Danielewicz and G. F. Bertsch, Nucl. Phys. A **533**, 712 (1991).
[47] Y. Oh, Z.-W. Lin, and C. M. Ko, Phys. Rev. C **80**, 064902 (2009).
[48] D. Oliinychenko, L.-G. Pang, H. Elfner, and V. Koch, Phys. Rev. C **99**, 044907 (2019).
[49] D. Oliinychenko, C. Shen, and V. Koch, Phys. Rev. C **103**, 034913 (2021).
[50] J. Staudenmaier, D. Oliinychenko, J. M. Torres-Rincon, and H. Elfner, Phys. Rev. C **104**, 034908 (2021).
[51] V. Kireyeu, J. Steinheimer, J. Aichelin, M. Bleicher, and E. Bratkovskaya, Phys. Rev. C **105**, 044909 (2022).
[52] G. Coci, S. Gläßel, V. Kireyeu, J. Aichelin, C. Blume, E. Bratkovskaya, V. Kolesnikov, and V. Voronyuk, Phys. Rev. C **108**, 014902 (2023).
[53] X.-Y. Zhao, Y.-T. Feng, F.-L. Shao, R.-Q. Wang, and J. Song, Phys. Rev. C **105**, 054908 (2022).

[54] R.-Q. Wang, J.-P. Lv, Y.-H. Li, J. Song, and F.-L. Shao, arXiv:2210.10271.
[55] R.-Q. Wang, F.-L. Shao, and J. Song, Phys. Rev. C **103**, 064908 (2021).
[56] T. Csörgő and B. Lörstad, Phys. Rev. C **54**, 1390 (1996).
[57] B. Tomášik and U. W. Heinz, Eur. Phys. J. C **4**, 327 (1998).
[58] R.-q. Wang, J. Song, G. Li, and F.-l. Shao, Chin. Phys. C **43**, 024101 (2019).
[59] L.-W. Chen, C. M. Ko, and B.-A. Li, Nucl. Phys. A **729**, 809 (2003).
[60] L. Zhu, C. M. Ko, and X. Yin, Phys. Rev. C **92**, 064911 (2015).
[61] I. Angeli and K. P. Marinova, At. Data Nucl. Data Tables **99**, 69 (2013).
[62] F. Bellini, K. Blum, A. P. Kalweit, and M. Puccio, Phys. Rev. C **103**, 014907 (2021).
[63] S. Mrowczynski, Acta Phys. Pol. B **48**, 707 (2017).
[64] A. Kisiel, M. Gałażyn, and P. Bożek, Phys. Rev. C **90**, 064914 (2014).
[65] J. Adam *et al.* (ALICE Collaboration), Phys. Rev. C **92**, 054908 (2015).
[66] J. Adam *et al.* (ALICE Collaboration), Phys. Rev. C **93**, 024905 (2016).
[67] A. Kisiel, W. Florkowski, W. Broniowski, and J. Pluta, Phys. Rev. C **73**, 064902 (2006).
[68] C. Alt *et al.* (NA49 Collaboration), Phys. Lett. B **685**, 41 (2010).
[69] V. Vovchenko, B. Dönigus, B. Kardan, M. Lorenz, and H. Stoecker, Phys. Lett. B **809**, 135746 (2020).
[70] S. Acharya *et al.* (ALICE Collaboration), Eur. Phys. J. C **77**, 658 (2017).
[71] P. Chakraborty, A. K. Pandey, and S. Dash, Eur. Phys. J. A **57**, 338 (2021).
[72] J. Adams *et al.* (STAR Collaboration), Phys. Rev. C **71**, 044906 (2005).
[73] B. Abelev *et al.* (ALICE Collaboration), Phys. Rev. C **88**, 044910 (2013).
[74] D. Oliinychenko, L.-G. Pang, H. Elfner, and V. Koch, MDPI Proc. **10**, 6 (2019).
[75] Y. Bailung, N. Shah, and A. Roy, Nucl. Phys. A **1037**, 122701 (2023).
[76] F.-X. Liu, Z.-L. She, H.-G. Xu, D.-M. Zhou, G. Chen, and B.-H. Sa, Sci. Rep. **12**, 1772 (2022).
[77] A. Kittiratpattana, T. Reichert, J. Steinheimer, C. Herold, A. Limphirat, Y. Yan, and M. Bleicher, Phys. Rev. C **106**, 044905 (2022).
[78] V. Gaebel, M. Bonne, T. Reichert, A. Burnic, P. Hillmann, and M. Bleicher, Eur. Phys. J. A **57**, 55 (2021).
[79] E. Schnedermann, J. Sollfrank, and U. W. Heinz, Phys. Rev. C **48**, 2462 (1993).
[80] S. Sombun, K. Tomuang, A. Limphirat, P. Hillmann, C. Herold, J. Steinheimer, Y. Yan, and M. Bleicher, Phys. Rev. C **99**, 014901 (2019).
[81] T. Reichert, J. Steinheimer, V. Vovchenko, B. Dönigus, and M. Bleicher, Phys. Rev. C **107**, 014912 (2023).